Applied Energy 330 (2023) 120350

Contents lists available at ScienceDirect

Applied Energy

journal homepage: www.elsevier.com/locate/apenergy

Favorable Start-Up behavior of polymer electrolyte membrane water electrolyzers

Edward Rauls [a,*], Michael Hehemann [a], Roger Keller [a], Fabian Scheepers [a], Martin Müller [a], Detlef Stolten [b,c]

[a] Forschungszentrum Juelich GmbH, Institute of Energy and Climate Research, IEK-14: Electrochemical Process Engineering, 52425 Juelich, Germany
[b] Forschungszentrum Juelich GmbH, Institute of Energy and Climate Research, IEK-3: Techno-economic System Analysis, 52425 Juelich, Germany
[c] RWTH Aachen University, Chair for Fuel Cells, Germany

HIGHLIGHTS

- Proposition of heat-up efficiency to evaluate start-up procedures energetically.
- Thermal parameters for electrolysis systems with up to 1 MW_{el} are presented.
- Efficiency when only using heating is always lower than partial-load heat-up.
- Introduction of a new dimensionless heat-up number for electrolyzers.
- Dimensionless heat-up number enables general estimation of time constants.

ARTICLE INFO

Keywords:
PEM electrolysis
Start-up
Heat-up
Efficiency
System modeling
Dynamic simulation

ABSTRACT

Dynamically-operated water electrolyzers enable the production of green hydrogen for cross-sector applications while simultaneously stabilizing power grids. In this study, the start-up phase of polymer electrolyte membrane (PEM) water electrolyzers is investigated in the context of intermittent renewable energy sources. During the start-up of the electrolysis system, the temperature increases, which directly influences hydrogen production efficiency. Experiments on a 100 kW_{el} electrolyzer, combined with simulations of electrolyzers with up to 1 MW_{el}, were used to analyze the start-up phase and assess its implications for operators and system designers. It is shown that part-load start-up at intermediate cell voltages of 1.80 V yields the highest efficiencies of 74.0 $\%_{LHV}$ compared to heat-up using resistive electrical heating elements, which reaches maximum efficiencies of 60.9 $\%_{LHV}$. The results further indicate that large-scale electrolyzers with electrical heaters may serve as flexible sinks in electrical grids for durations of up to 15 min.

1. Introduction

Energy storage technologies constitute valuable tools for overcoming the critical problems facing energy systems with large shares of renewable energy sources (RES). Currently, the main large-scale energy storage technology is pumped hydro power (PHS). The storage of surplus energy for potential use is efficient and well established, but eligible land for the further deployment of this technology is limited [1]. Additionally, PHS is unable to offer the highly dynamic responses necessary for frequency containment grid services, although advanced PHS plants carry the potential for increased flexibility [2]. High-frequency voltage control services can also be provided by flywheels [3] and supercapacitor storage [4], but the low energy density of these technologies limits their large-scale application. In compressed air energy storage (CAES), surplus electricity is used to pump air into underground reservoirs such as salt caverns, aquifers, or depleted natural gas reservoirs. re-electrification is then achieved by expanding the gas in turbines [5]. The limited availability of suitable storage cavities hinders the widespread application of the CAES technology, however [5]. Battery storage is a rapidly expanding field with potential for smart management of distributed storage, such as for battery–electric vehicles or stationary systems [6]. Power-to-gas (PtG) technologies aim to produce

---

* Corresponding author.
E-mail address: e.rauls@fz-juelich.de (E. Rauls).

https://doi.org/10.1016/j.apenergy.2022.120350
Received 15 September 2022; Received in revised form 29 October 2022; Accepted 14 November 2022

gaseous platform energy carriers, such as methane, ammonia, or other synthetic fuels, using excess electricity. Hydrogen from water electrolysis is the principal feedstock of PtG processes, especially with limited CO_2 storage capacities, and could account for up to 50 % of future electricity demand [7]. Although PtG may currently not be economically-profitable, the future development of electricity prices may change this situation [8]. With its potential for seasonal storage, PtG could contribute to 5 % of annual energy demand by storing excess electricity during the summer for covering winter peak demands [9].

Water electrolysis has the potential to serve as a central link in the energy field. The principal water electrolysis technologies are alkaline, acidic, and solid oxide [10]. Polymeric electrolyte membrane (PEM) electrolyzers can be operated under intermittent and variable loads typical for power from RES and electrochemically produce hydrogen from water and electricity. Hydrogen can then be stored on a large scale, for example in salt caverns. The flexibility of PEM electrolyzers can help to substantially reduce the greenhouse gas emissions of the transportation sector when compared to conventional fuels by capturing transient energy from RES [11]. Hydrogen transport in pipelines can also be economically-favorable to electricity transport over the grid and can even support electricity grid expansion processes by reducing grid congestion and the curtailment of green electricity [12]. Water electrolyzers can increase the profitability of existing renewable energy systems if their operating times are sufficiently high [13]. Other short-term business cases lie in the replacement of gray hydrogen from fossil sources to reduce the carbon footprint of industrial processes such as oil refining [14], metallurgy [15], or fertilizer production [16]. Although the high cost of electrolysis systems has been the main inhibitor to the broad application of PEM water electrolyzers thus far, cost studies indicate that its investment costs approach the level of alkaline electrolyzers [17]. Innovative process configurations and novel materials are developed continuously to increase efficiency and lower costs [18]. The competitive advantages of PEM systems, owing to their higher flexibility, are expected to cause a shift towards their large-scale usage in the future [19]. Overall, operating scenarios with repeated on–off cycles of electrolysis systems due to the inherent dynamics of RES are gaining importance. Hence, the start-up behavior of PEM electrolyzers is investigated in this article.

2. Theoretical background

2.1. Polarization of electrolysis cells

Hydrogen can be produced electrochemically by splitting water into its constituent components of hydrogen and oxygen, as stated in (1):

$$\mathbf{H_2O \rightarrow H_2 + \frac{1}{2}O_2} \tag{1}$$

Regardless of the electrolyzer technology utilized, the water splitting reaction requires the reaction enthalpy ΔH. This property is determined by the change in the Gibbs energy ΔG, which must be supplied as electrical energy, and the product of the temperature and change in entropy $T\Delta S$, which can be provided as heat, as specified in (2). Under standard conditions, the change in reaction enthalpy makes up 285.84 kJ mol^{-1} and the change in Gibbs energy is 237.15 kJ mol^{-1} [20]:

$$\Delta H = \Delta G + T\Delta S \tag{2}$$

Electrochemical reactions proceed if the voltage applied to the cell exceeds a specific threshold. Cell voltages are also used to evaluate the inherent efficiency and material requirements of electrochemical devices. They can be calculated from the reaction enthalpy E and Gibbs enthalpy G using equation (3), where z is the number of transferred electrons (for water electrolysis $z = 2$) and F is the Faraday constant ($F = 96485\ \mathrm{A\,s\,mol^{-1}}$). Inserting the standard reaction enthalpy of the water splitting in (3) results in the so-called thermoneutral voltage of 1.48 V. This is the minimum voltage that is required to split water if no additional heat is provided to the reaction. Inserting the change in Gibbs energy yields a reversible cell voltage of 1.23 V for splitting liquid water if heat is drawn from the reaction environment.

$$U = \frac{E}{z\mathrm{F}} \tag{3}$$

The Nernst voltage defines the required cell voltage of an ideal water splitting reaction without losses and is given by (4). It encompasses the influence of temperature on the Nernst voltage through an empirical expression for the reversible voltage by Harrison et al. [21] and a pressure-dependent correction term that accounts for changes in thermodynamic fugacity and activity if an ideal solution and the Henry law are assumed to be applicable [22]. Within the logarithmic expression, the partial pressures of oxygen and hydrogen are normalized to the reference pressure of 1 bar and the result is exponentiated by the respective stoichiometric coefficient of each component from (1):

$$U_{\mathrm{nernst}} = U_{\mathrm{rev}}(T) + \frac{\mathrm{R}T_{\mathrm{cell}}}{2\mathrm{F}} \cdot ln\left(\sqrt{\frac{p_{\mathrm{O_2}}}{p_0}} \cdot \frac{p_{\mathrm{H_2}}}{p_0}\right) \tag{4}$$

In addition to the thermodynamically-minimal required voltages, electrolysis cells need further overpotentials η to execute the water splitting reaction. The cell voltage U_{cell} is the sum of the Nernst voltage U_{nernst}, activation overpotential η_{act}, Ohmic overpotential η_{ohm}, and concentration overpotential η_{conc}, as given by (5):

$$\boldsymbol{U_{\mathrm{cell}} = U_{\mathrm{nernst}} + \eta_{\mathrm{act}} + \eta_{\mathrm{ohm}} + \eta_{\mathrm{conc}}} \tag{5}$$

The activation overpotential provides the necessary kinetic energy for electrochemical reactions and primarily depends on temperature and the utilized catalysts. The Butler–Volmer equation (equation (6)) states the dependency of the current density j from the applied cell overpotential η at the electrodes relative to the equilibrium potential. Cathode and anode have individual exponential terms that contain separate charge transfer coefficients α_{an} and α_{cat}. Additionally, the activation overpotential is proportional to the exchange current density j_0:

$$j = j_0 \cdot \left[\exp\left(\frac{\alpha_{\mathrm{an}} z\mathrm{F}}{\mathrm{R}T}\eta\right) - \exp\left(-\frac{\alpha_{\mathrm{cat}} z\mathrm{F}}{RT}\eta\right)\right] \tag{6}$$

Assuming a negligible cathode potential, which is valid for PEM water electrolysis due to the low cathode potential relative to the anode potential [23], the Butler–Volmer equation can be simplified and rearranged to obtain the current density-dependent Tafel expression in (7). Often, a charge transfer coefficient of 0.5 is assumed, but other values have been reported depending on the operating temperature and utilized materials [24].

$$\eta_{\mathrm{act}} = \frac{\mathrm{R}T}{2\mathrm{F}\alpha} ln\left(\frac{j_{\mathrm{cell}}}{j_0}\right) \tag{7}$$

Ohmic overpotentials result from the electric current and proton flow through the polymeric membrane. In **(8)**, the contributions of electric conductors and contact resistances are contained in R_Ω and the ionic resistance of the membrane is described by $R_{\mathrm{mem}}(T)$:

$$\boldsymbol{\eta_{\mathrm{ohm}} = j_{\mathrm{cell}} \cdot (R_{\mathrm{mem}}(T) + R_\Omega)} \tag{8}$$

The transport of protons through the membrane during water electrolysis entails ohmic losses that are governed by the protonic conductance of the membrane. Membrane thickness d_{mem} and temperature-dependent protonic conductivity $\sigma_{\mathrm{mem}}(T)$ contribute to the losses, as stated in (9). Therefore, reducing the membrane thickness, increasing the protonic conductance, and more temperature-resistant membrane materials are important fields of research and development in water electrolysis.

$$\boldsymbol{R_{\mathrm{mem}}(T) = \frac{d_{\mathrm{mem}}}{\sigma_{\mathrm{mem}}(T)}} \tag{9}$$

Several models have been proposed to describe the proton conductivity of Nafion™ membranes in fuel cells and water electrolyzers. Of those, the model by Springer et al. [25] has found widespread application. Although it is easy to apply numerically, membrane humidity is non-trivial to quantify for water electrolysis regimes [26] and a wide range of values has been utilized in the literature [27]. In this article, the model by Yadav et al. [28] according to (10) is preferred, as it uses the thermodynamic activity and temperature of the water that is in contact with the membrane. For fully hydrated membranes and the splitting of liquid water, an activity of 1 can be assumed.

$$\boldsymbol{\sigma}_{\mathbf{mem}}(\boldsymbol{T}, \boldsymbol{a}_{\mathrm{w}}) = (0,6877 + \boldsymbol{a}_{\mathrm{w}})\,\mathbf{exp}\left\{-\frac{10440\cdot\boldsymbol{a}_{\mathrm{w}}^{-1/4}}{\mathbf{R}\boldsymbol{T}}\right\} \tag{10}$$

Mass transfer overpotentials arise from the suboptimal provision of water to the electrolysis cell and the incomplete removal of product gases from the electrodes, resulting in the partial starvation of electrochemically-active cell sections. Correct cell and stack design, as well as correct operation, mitigate mass transfer overpotentials – even at current densities above 10 A cm^{-2} [29].

2.2. *Thermal properties of water electrolyzers*

Water electrolyzers are frequently modeled in isothermal conditions to reduce model complexity. Although this simplification is valid when studying steady-state operation, temperature-dependent properties are crucial for dynamic simulations. The first dynamic thermal model for electrolyzers was presented by Ulleberg [30] in 2003. As conveyed in (11), this model uses the lumped thermal capacitance C_{th} to provide thermal inertia to the system. The change in temperature further depends on the enthalpy streams entering and exiting the electrolyzer, as well as the heat balance.

$$C_{\mathrm{th}}\frac{dT}{dt} = \sum_i \dot{m}_i h_i + \sum_j \dot{Q}_j \tag{11}$$

The thermal capacitance of a subsystem is composed of the products of the respective masses of its constituent materials and their heat capacities, as given in (12). Subsystems are aggregated to the entire system based on the rules for capacitors in electrical circuits [31].

$$C_{\mathrm{th}} = \sum_k m_k c_{p,k} \tag{12}$$

Heat losses to ambient are represented by thermal resistances, which consist of the contributions of the surfaces with convective heat transfer coefficients, as per (13). The equivalent resistance of the entire system is composed analogously to the treatment of ohmic resistances in electrical circuits.

$$R_{\mathrm{th}} = \sum_l (\alpha_l S_{\mathrm{th},l})^{-1} \tag{13}$$

Using the equivalent thermal resistance, the heat losses $\dot{Q}_{\mathrm{loss}}$ are calculated from the temperature difference between the interior of the water electrolyzer T and ambient temperature T_{amb} using (14). This simplified approach allows for an intuitive model that includes transient thermal system responses.

$$\dot{Q}_{\mathrm{loss}} = \frac{1}{R_{\mathrm{th}}}(T - T_{\mathrm{amb}}) \tag{14}$$

Multiplication of the thermal capacitance and the thermal resistance of a system yields the thermal time constant τ_{th}, (15). The thermal time constant describes the time a system requires for its temperature to drop by 36.8 % of the initial temperature due to convective heat losses with no further heat input [31].

$$\tau_{\mathrm{th}} = C_{\mathrm{th}} \cdot R_{\mathrm{th}} \tag{15}$$

The thermal time constant offers a temporal description of the thermal system's behavior and combines information on heat capacity and losses.

3. Materials and methods

3.1. *Experimental investigation of electrolyzer start-up*

The experiments for this study were performed using a fully in-house-developed and constructed electrolyzer with a maximum electrical power draw of 100 kW$_{\mathrm{el}}$. Hydrogen production at 50 bar with equal or differential pressures is possible. For the presented experiments, the gas pressure on the hydrogen side was 6 bar and 5 bar on the oxygen side, which are required on the reference test station due to minimum pressure demands of the installed hydrogen in oxygen gas sensor. These pressure levels are furthermore interesting for industrial applications, since hydrogen production at intermediate pressure can save compression stages and still offers reasonable cell efficiencies [32]. To achieve the power rating, two identical electrolysis stacks were electrically-connected in parallel, encompassing 27 cells each with a geometric area of 300 cm^2. The utilized membrane electrode assembly consisted of a Nafion™ 117 membrane, iridium catalyst (2.6 mg cm^{-2}) on the anode side, and a platinum catalyst on the cathode side (0.9 mg cm^{-2}). A 100 kW$_{\mathrm{el}}$ insulated-gate bipolar transistor DC power supply (aixcon PowerSystems) provided electric power to the stacks. Electric cartridge heaters (Türk + Hillinger) provided up to 4 kW$_{\mathrm{th}}$ of heat to the anodic and cathodic water cycles. Plate heat exchangers (AlphaLaval), each with 18 kW$_{\mathrm{th}}$ ratings, supplied cooling to the electrolyzer.

3.1.1. *Heat-up experiments*

At the 100 kW$_{\mathrm{el}}$ test station, a heat-up from 25 °C to 75 °C was investigated. Stack heat-up was quantified with the arithmetic mean temperature at the outlets of the electrolysis stacks. Different heat-up strategies can be employed during electrolyzer start-up to achieve the operating temperature. In low-temperature water electrolysis, heat can be supplied by three main strategies: electrical resistance heating, waste heat from the electrochemical water splitting reaction, or a combination of both. Experiments were performed to identify the most efficient approach and determine the typical heat-up ramps of water electrolyzers. Table 1 provides an overview of the studied strategies and their experimental parameters.

Firstly, heat-up solely via cartridge heating was investigated. Secondly, potentiostatic part-load operation at 1.80 V was used, once with and once without the 4 kW$_{\mathrm{th}}$ heating. By defining the permissible cell voltage during heat-up, accelerated cell degradation can be reduced [33]. 1.80 V was selected for the potentiostatic experiments since it is a likely cell voltage for favorable electrolyzer start-up. At this voltage, the heat input is substantial compared to lower voltages while still maintaining a sufficient hydrogen production efficiency. Thirdly, two separate galvanostatic strategies were tested, in which the applied current density was increased at predefined temperatures. All galvanostatic strategies included additional electric heating. The two-step galvanostatic strategy starts with electric heating to 40 °C, at which a current

Table 1
Parameters of the investigated heat-up strategies for the 100 kW$_{\mathrm{el}}$-test station.

Strategy	Operating parameter	Heating power	Temperature range
Heating only	0,00 V	4 kW$_{\mathrm{th}}$	25 °C – 75 °C
Potentiostatic	1,80 V	0 kW$_{\mathrm{th}}$	25 °C – 75 °C
	1,80 V	4 kW$_{\mathrm{th}}$	25 °C – 75 °C
Galvanostatic	0,0 A cm^{-2}	4 kW$_{\mathrm{th}}$	25 °C
two steps	0,5 A cm^{-2}	4 kW$_{\mathrm{th}}$	40 °C
	1,0 A cm^{-2}	4 kW$_{\mathrm{th}}$	60 °C – 75 °C
Galvanostatic	0,0 A cm^{-2}	4 kW$_{\mathrm{th}}$	25 °C
three steps	0,5 A cm^{-2}	4 kW$_{\mathrm{th}}$	40 °C
	1,0 A cm^{-2}	4 kW$_{\mathrm{th}}$	50 °C
	1,5 A cm^{-2}	4 kW$_{\mathrm{th}}$	60 °C – 75 °C

density of 0.50 A cm^{-2} was applied. After reaching 60 °C, the current density was increased to 1.50 A cm^{-2}. The three-step strategy started identically with heat-up to 40 °C by the heating cartridges and respective current density steps of 0.50 A cm^{-2}, 1.00 A cm^{-2}, and 1.50 A cm^{-2} at 40 °C, 50 °C, and 60 °C.

Heat-up with fixed heat input is the basic benchmark since the heat input can be fully controlled. Galvanostatic operation with limited current density steps represents the manual operation of electrolyzers during accelerated heat-up by increasing the applied current density in discrete steps at specific temperatures. The two separated galvanostatic strategies have been analyzed to show the influence of additional steps on the heat-up. Furthermore, the potentiostatic strategy represents the same basic idea of increasing the current density with temperature, but with an infinite number of steps.

3.1.2. *Polarization experiments*

During the start-up process of water electrolyzers that include part load operation, electrochemical and thermal properties change with the cell temperature. In particular, the exchange current density and charge transfer coefficient, as defined in (16), must be determined to obtain simulation parameters. Therefore, polarization curves at operating temperatures between 25 °C and 75 °C were measured in the reference electrolyzer. The gas pressures were 6 bar on the cathode side and 5 bar on the anode one, with a water recirculation rate of 15.75 l min^{-1} on both sides. Each current density point was held constant for at least 30 min after the operating temperatures stabilized and the mean cell voltage was determined.

$$i_0(T) = i_{0,\mathrm{ref}} \cdot \exp\left(-\frac{E_{\mathrm{A}}^{i_0}}{RT}\right) \tag{16}$$

$$\alpha_0(T) = \alpha_{0,\mathrm{ref}} \cdot \exp\left(-\frac{E_{\mathrm{A}}^{\alpha}}{RT}\right) \tag{17}$$

Arrhenius-type temperature-dependent expressions for the exchange current density and charge transfer coefficient were assumed, as stated in (16) and (17). For the exchange current density, this assumption was reported in [34] using an activation energy $E_{\mathrm{A}}^{i_0}$ of 40 kJ mol^{-1} from [35]. From the cell polarization data, individual values at each temperature were determined using the least square regression method. The results were consistent with an Arrhenius-type temperature dependency for the charge transfer coefficient, with an activation energy E_{A}^{α} of 3.4 kJ mol^{-1}.

3.2. *Energetic comparison of start-up strategies*

Hydrogen production in part-load operation during heat-up must be considered to enable a comparison of heat-up strategies that purely rely on electrical heating. Therefore, the energy expenditure for heating $E_{\mathrm{ht,heat-up}}$ and for the hydrogen production $E_{\mathrm{el,heat-up}}$ must be quantified. Accordingly, the total energy demand is given by (18). The time integral over the momentary heating input from t_0 to $t_{\mathrm{heat-up}}$ yields $E_{\mathrm{ht,heat-up}}$, (19), where t_0 is the beginning of the experiment, when the stack temperature is 25 °C and $t_{\mathrm{heat-up}}$ is the time at which the stack temperature reaches its operating level, here 75 °C. Similarly, the energy for electrolysis $E_{\mathrm{el,heat-up}}$ is calculated in (20) from the stack voltage U_{stack} and current I_{stack} and added up for both stacks of the test station. As either voltage or current change during the investigated start-up strategies, the time integrals provide full information during heat-up. Correspondingly, the mass of produced hydrogen $m_{\mathrm{H_2,heat-up}}$ is determined through the time integral of the momentary hydrogen mass flow rate $\dot{m}_{\mathrm{H_2}}(t)$, (21). Subsequent multiplication of $m_{\mathrm{H_2,heat-up}}$ with the lower heating value (LHV) of hydrogen $LHV_{\mathrm{H_2,wt}}$ yields its energy content. From the total energy demand for start-up $E_{\mathrm{heat-up}}$, the energy in the storable hydrogen produced $E_{\mathrm{H_2,heat-up}}$, and the heat-up duration $\Delta t_{\mathrm{heat-up}}$, the mean heat input $\dot{Q}_{\mathrm{mean}}$ can be quantified, (22). This value enables a comparison of the thermal aspects of different heat-up strategies.

$$E_{\mathrm{heat-up}} = E_{\mathrm{ht,heat-up}} + E_{\mathrm{el,heat-up}} \tag{18}$$

$$E_{\mathrm{ht,heat-up}} = \int_{t_0}^{t_{\mathrm{heat-up}}} \dot{Q}_{\mathrm{HT}}(t)dt \tag{19}$$

$$E_{\mathrm{el,heat-up}} = \int_{t_0}^{t_{\mathrm{heat-up}}} \left(\sum_{j=1}^{n_{\mathrm{stacks}}} U_{\mathrm{stack},j}(t) \cdot I_{\mathrm{stack},j}(t)\right)dt \tag{20}$$

$$E_{\mathrm{H_2,heat-up}} = \int_{t_0}^{t_{\mathrm{heat-up}}} \dot{m}_{\mathrm{H_2}}(t)dt \cdot LHV_{\mathrm{H_2,wt}} = m_{\mathrm{H_2,heat-up}} \cdot LHV_{\mathrm{H_2,wt}} \tag{21}$$

$$\dot{Q}_{\mathrm{mean}} = \frac{E_{\mathrm{heat-up}} - E_{\mathrm{H_2,heat-up}}}{\Delta t_{\mathrm{heat-up}}} \tag{22}$$

The influence of the heat-up strategy diminishes with operation duration, and it cannot be compared absolutely. Selecting a fixed quantity for the relative comparison, however, enables a measure of the heat-up efficiency to be made, which is especially valuable in the case of repeated start–stop cycles. The maximum amount of produced hydrogen during all start-up strategies $m_{\mathrm{H_2,max}}$ is determined and the residual $m_{\mathrm{H_2,res}}$ between this reference quantum and the respective hydrogen production $m_{\mathrm{H_2,heat-up}}$ is separately calculated for each strategy using (23). Based on the hydrogen residual, the required energy E_{res} to produce the full hydrogen quantum under nominal conditions is calculated, (24). Thereby, the start-up phase consists of the heat-up phase and residual production phase. Furthermore, the time for this residual production t_{res} is determined by the hydrogen mass flow at nominal conditions $\dot{m}_{\mathrm{H_2,nom}}$, (25). The total start-up time t_{total} then consists of the heat-up time and the duration needed to produce the hydrogen residuum, (26).

$$m_{\mathrm{H_2,res}} = m_{\mathrm{H_2,max}} - m_{\mathrm{H_2,heat-up}} \tag{23}$$

$$E_{\mathrm{res}} = \frac{m_{\mathrm{H_2,res}} \cdot LHV_{\mathrm{H_2,wt}}}{\eta_{\mathrm{nom}}} \tag{24}$$

$$t_{\mathrm{res}} = m_{\mathrm{H_2,res}} / \dot{m}_{\mathrm{H_2,nom}} \tag{25}$$

$$t_{\mathrm{total}} = t_{\mathrm{heat-up}} + t_{\mathrm{res}} \tag{26}$$

The nominal operating conditions were 1.80 V (1.75 Acm^{-2}) at 75 °C, 6 bar cathodic gas pressure, 5 bar anodic gas pressure, and a recirculation rate of 15.75 l min^{-1}. The electrolyzer efficiency under these conditions η_{nom} based on the lower heating value was found to be 68.3 %$_{\mathrm{LHV}}$ at a hydrogen production of 0.76 kg h^{-1}.

$$\eta_{\mathrm{heat-up}} = \frac{m_{\mathrm{H_2,max}} \cdot LHV_{\mathrm{H_2,wt}}}{E_{\mathrm{heat-up}} + E_{\mathrm{res}}} \tag{27}$$

In addition to these absolute values, the dimensionless start-up efficiency can be defined by utilizing (27), which describes the amount of energy required to produce the hydrogen reference quantum and the energy for heat-up and electrolysis operation.

$$\mathrm{E} = \frac{C_{\mathrm{th}} \cdot \Delta T}{\tau_{\mathrm{th}} \cdot \dot{Q}_{\mathrm{mean}}} \tag{28}$$

$$\Delta T = T_{\mathrm{nom}} - T_0 \tag{29}$$

$$t' = \frac{t_{\mathrm{heat-up}}}{\tau_{\mathrm{th}}} \tag{30}$$

Finally, a new dimensionless number is presented to combine the energetical and temporal evaluation of heat-up strategy for different electrolysis systems. This heat-up number E is defined by (28) and sets the stored thermal energy in the electrolyzer in proportion to the heat injected during heat-up. Depending on the starting temperature T_0 and nominal operating temperature T_{nom}, the rise of temperature ΔT during heat-up is given by (29). From the heat-up time and thermal time constant, the dimensionless heat-up time is calculated from (30). The dimensionless heat-up number and heat-up time can be used to evaluate how effective the start-up strategies are.

3.3. Simulation of electrolyzer start-up

3.3.1. Simulation equations

Electrolyzer heat-up was simulated in a MATLAB-Simulink using a simplified thermal model based on (11) and experimentally-determined parameters. The heat balance of water electrolyzers during heat-up is composed of heating and cooling effects, (31). Overvoltages during electrolysis cause Joule heating $\dot{Q}_{OV}$, which is proportional to the applied current and the difference between the cell voltage U_{cell} and thermoneutral voltage U_{th}, (32). Temperature and pressure influence the thermo-neutral voltage, which is considered by implementing the data from [36] into the simulation model. If the electrolyzer contains resistive heating elements, a controlled heat input $\dot{Q}_{HT}$ can be achieved. In this case, a separation of heat-up and electrolysis operation is possible, whereby the electrolyzer effectively acts as a heat sink. During electrolysis, the saturation of the product gases with water vapor induces a cooling effect $\dot{Q}_{vap}$ that is temperature- and pressure-dependent, as described in (33). The operating temperature influences the saturation pressure of water vapor in the gases and the heat of vaporization that causes the cooling effect. The gas pressures on the cathode and anode sides determines the loading of the gas streams for a fixed relative humidity φ. For the simulations reported in this article, full saturation of the gas streams is assumed ($\varphi = \varphi^{cat} = \varphi^{an} = 1$). Species balances for the anode and cathode compartments yield the gas flow rates for hydrogen and oxygen, which are given by (34) and (35). Convective heat losses to ambient are simulated from (14) with a constant ambient temperature of 25 °C.

$$\sum_j \dot{Q}_j = \dot{Q}_{OV} + \dot{Q}_{HT} - \dot{Q}_{vap} - \dot{Q}_{loss} \tag{31}$$

$$\dot{Q}_{OV} = I_{stack}\left(U_{cell} - U_{th}(T)\right) \tag{32}$$

$$\dot{Q}_{vap} = \left[\dot{n}_{H_2}\frac{p_{s,H_2O}(T)}{\frac{p^{cat}}{\varphi^{cat}} - p_{s,H_2O}(T)} + \dot{n}_{O_2}\frac{p_{s,H_2O}(T)}{\frac{p^{an}}{\varphi^{an}} - p_{s,H_2O}(T)}\right]\Delta h_{vap,H_2O}(T) \tag{33}$$

The permeation of hydrogen and oxygen through the electrolytic membrane causes deviations from the ideal gas production rates according to Faraday's law. The first term on the right side of (34) represents Faraday's law and the other terms consider the permeative losses of hydrogen. Permeation is determined by the permeability of the species through Nafion™ membranes, which was investigated thoroughly for fuel cell and electrolysis applications [37]. The recombination of permeated oxygen from the anode compartment to water on the platinum-based catalyst on the cathode side leads to additional hydrogen losses. Permeated hydrogen, however, does not react at the iridium-based catalyst at the anode, resulting in the oxygen production rate given by (35). Permeability increases with temperature and varies with the respective species. Thicker membranes reduce gas permeation, and the partial pressure of the species drive their crossover.

$$\dot{n}_{H_2} = \frac{n_{cell} \cdot j_{cell} \cdot A_{cell}}{2F} - P_{H_2}(T)\frac{p^{cat}_{H_2}}{d_{mem}} - 2P_{O_2}(T)\frac{p^{cat}_{O_2}}{d_{mem}} \tag{34}$$

$$\dot{n}_{O_2} = \frac{n_{cell} \cdot j_{cell} \cdot A_{cell}}{4F} - P_{O_2}(T)\frac{p^{cat}_{O_2}}{d_{mem}} \tag{35}$$

$$p^{cat}_{H_2} = p^{cat} - p_{s,H_2O}(T) \tag{36}$$

$$p^{an}_{O_2} \approx p^{an} - p_{s,H_2O}(T) \tag{37}$$

The partial pressure of hydrogen is given by (36) from the total pressure on the cathode minus the saturation pressure of water at the cell temperature. On the anode side, the oxygen partial pressure is approximated in the same way, neglecting the partial pressure of permeated hydrogen, as per (37). This assumption is valid given that the hydrogen content in the anodic gas streams is typically kept below 2 vol % for safety reasons [38].

3.3.2. Simulation parameters

3.3.2.1. Electrochemical parameters. Fig. 1 a) illustrates the polarization curves of the reference electrolyzer in this study for temperatures between 25 °C and 75 °C. Cell voltages at a fixed current density decrease with increasing temperature due to the lower protonic transport resistance of the electrolytic membrane, better kinetics, and lower reversible cell voltage. The data points in Fig. 1 a) represent the measurement data points and lines given by the simulated cell polarization, based on the extracted electrochemical cell parameters from Fig. 1 b). Although a temperature-independent Ohmic cell resistance of 7 mΩ was determined, the charge transfer coefficient and exchange current density were found to be temperature-dependent. The exchange current density exhibits a stronger temperature dependency than the charge transfer coefficient and increases almost tenfold, from $7.1 \bullet 10^{-7}$ A cm^{-2} at 25 °C to $7.0 \bullet 10^{-6}$ A cm^{-2} at 75 °C. Meanwhile, the charge transfer coefficient changes from 0.386 to 0.469 in the same temperature interval, which is in good agreement with the frequently assumed value of 0.50 at temperatures of around 80 °C.

These electrochemical parameters were then used to predict the polarization of electrolysis cells with thinner membranes of 50 μm. Based on these state-of-the-art electrolysis cells, stacks for electrolysis systems with nominal electrical power uptakes of up to 1 MW$_{el}$ were designed. Table 2 provides an overview of the parameters that were used during the scale-up process. Up to a nominal stack power of 400 kW$_{el}$, parameters from existing electrolyzers at the IEK-14 were used. Scaling further to 1 MW$_{el}$, the cell area was extrapolated to 3000 cm^2 to include potential economies of scale benefits during cell and stack manufacturing. Nominal operating conditions were assumed to be 75 °C, 6 bar gas pressure on the cathode side, and 5 bar on the anode side. Nominal cell voltages and current densities determined the number of cells for each stack and are listed in Table 2.

In addition to the cells of the reference electrolyzer of this study, which uses conservative Nafion™ 117 membranes with a thickness of 200 μm, the same design was modeled with 50 μm membranes to facilitate comparison with the other simulations. Furthermore, heating powers were defined for each electrolyzer in such a way that the heating would be sufficient to maintain a cell temperature of 80 °C.

3.3.2.2. Thermal parameters. Heat-up simulations for electrolyzers at different scales require detailed thermal parameters. Typical PEM electrolysis stacks consist of multiple repetition units that are made of stainless steel, titanium, copper, and polymers. Endplates, bipolar plates, and peripheral components such as pipes and gas–water separator tanks are usually manufactured from stainless steel. Polymers are used for electrical insulation of the cell frames to prevent electrical shortcuts. The weight-specific heat capacities for these materials are listed in Table 3. Heat transfer mainly occurs through either the stainless steel of endplates and peripherals or through the polymeric interfaces of the stacks. The associated heat transfer coefficients for stainless steel and polymeric surfaces were determined in the test station based on the methodology of [39] and are assumed to be 21 W m^{-2} K^{-1} and 2.1 W m^{-2} K^{-1}, respectively.

The lumped thermal capacity and resistances of electrolysis stacks and systems were then derived from existing electrolyzers up to electrical power ratings of 400 kW$_{el}$. Additionally, electrolyzers with nominal power ratings of 750 kW$_{el}$ and 1 MW$_{el}$ were designed by extrapolating the components. With respect to the cell and stack components, the dimensions and masses were scaled according to the cell

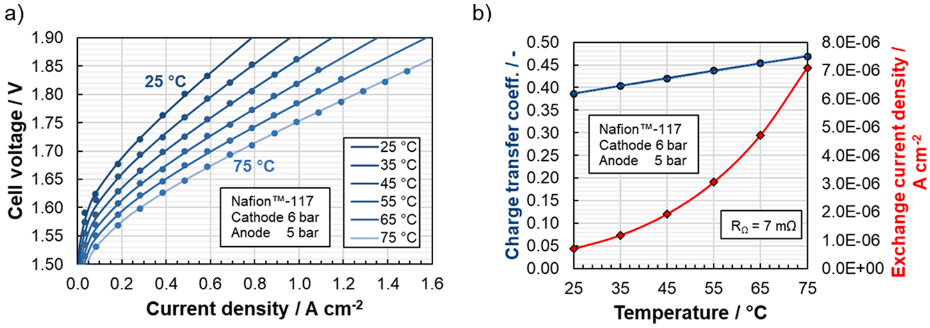

Fig. 1. Electrolysis cell polarization model for Nafion™ 117 membranes at 6 bar pressure on the cathode side, 5 bar on the anode side with temperatures between 25 °C and 75 °C: a) Polarization curves with experimental values (dots) and simulated values (lines); b) charge transfer coefficients (blue) and exchange current densities (red) fitted to the experimental data. (For interpretation of the references to colour in this figure legend, the reader is referred to the web version of this article.)

Table 2

Scale-up parameters used for the simulation of electrolyzers with power ratings between 5 kW_{el} and 1 MW_{el}. *For the simulations of the 100 kW_{el} electrolyzer, 50 µm membranes were assumed to facilitate comparison with the other systems, whereas the reference test station used 200 µm membranes.

Nominal power	Membrane thickness	Cell area	Number of cells	Current density	Cell voltage	Heating
kW_{el}	µm	cm^2	–	A cm^{-2}	V	kW_{th}
5	50	100	8	3.50	1.79	2
50	200* / 50	300	27	3.00* / 3.50	2.06* / 1.79	4
400	50	1056	73	3.00	1.75	12
750	50	2220	64	3.00	1.75	18
1000	50	3000	53	3.50	1.79	25

Table 3

Heat capacities and heat transfer coefficients of the materials constituting electrolysis stack and system components.

Material	Heat capacity	Source	Heat transfer coefficient	Components
	J kg^{-1} K^{-1}		W m^{-2} K^{-1}	–
Stainless steel	500	[40]	21.00	Endplates, bipolar plates, peripherals
Copper	385	[41]	–	Current collectors
Polymer	1250	[42]	2.10	Frames, insulation
Water	4185	[43]	–	Stack, peripherals

area and number of cells from Table 2. Peripheral system components were designed by maintaining the geometric similarity. The results of the scale-up process regarding the masses of stack and peripheral components and their respective thermal surfaces are listed in Table 4. Aside from the dry mass, the water contained within of the components contributes significantly to the lumped heat capacity.

Fig. 2 a) illustrates the thermal parameters for the cell stacks. Up to nominal power ratings of 400 kW_{el}, a linear relationship between the nominal power and lumped thermal capacity is observed. The thermal capacitance of the electrolysis stacks, including the water content, increases from 16.2 kJ K^{-1} for a 5 kW_{el} stack to 421.0 kJ K^{-1} for a 400 kW_{el} one. At higher scales, the thermal capacitance increases less steeply and makes up 752.0 kJ K^{-1} for the 1 MW_{el} stack, including the water content. Dissipative heat losses increase with the scale, which decrease the thermal resistances of bigger stacks. Although the thermal resistances of smaller stacks are higher, with 377.7 K kW^{-1} at 5 kW_{el} and 159.2 K kW^{-1} at 50 kW_{el}, the resulting heat losses relative to the heat production within the electrolytic cells are nonetheless higher than in larger stacks. Accordingly, maintaining high operating temperatures is much more challenging in smaller electrolysis stacks that tend to cool down faster than larger ones, as the relationship between the mass, power density, and thermal surfaces changes. Although the thermal resistance decreases to 31.9 K kW^{-1} at 1 MW_{el}, the electrochemical heat production exceeds these heat losses under nominal conditions, making cooling a difficult thermal management operation.

The thermal properties of the stack and the balance of plant amount to the thermal properties of the total electrolysis system, as depicted in Fig. 2 b). All peripheral components scale with the nominal power rating of the electrolyzer, increasing the thermal capacity almost linearly from 51.6 kJ K^{-1} at 5 kW_{el} to 1434.3 kJ K^{-1} at 400 kW_{el} and to 2848.6 kJ K^{-1} at 750 kW_{el}. With 4407.5 kJ K^{-1}, the 1 MW_{el} system lies slightly over the linear trend of the other systems, which is caused by the water content of the peripheral components such as pipes and gas–water separator vessels. Qualitatively, the thermal resistances of the systems develop similarly to the stacks, decreasing with scale due to their larger thermal surfaces, especially of the peripherals. Quantitatively, the thermal resistances are lower, ranging from 39.7 K kW^{-1} at 5 kW_{el}, to 5.0 K kW^{-1} at 400 kW_{el}, to 2.3 K kW^{-1} at 1 MW_{el}.

3.3.3. *Simulation configurations*

In section 4.2.1, electrolyzer heat-up with constant heat-input is simulated for a 400 kW_{el} system with heating powers between 12 kW_{th} and 80 kW_{th}. In section 4.2.2 heat-up with constant heat input is

Table 4

Masses and thermal surfaces of the materials for electrolysis stacks and peripheral components of electrolyzers with power ratings between 5 kW_{el} and 1 MW_{el}.

	Stacks						Peripherals		
P_{nom}	m^{stack}_{steel}	m^{stack}_{copper}	$m^{stack}_{titanium}$	$m^{stack}_{H_2O}$	$S^{stack}_{th,steel}$	$S^{stack}_{th,PEEK}$	m^{periph}_{steel}	$m^{periph}_{H_2O}$	$S^{periph}_{th,steel}$
kW_{el}	kg	kg	kg	kg	m^2	m^2	kg	kg	m^2
5	23.8	2.1	0.3	0.8	0.11	0.05	52.5	8.1	0.98
50	80.0	6.7	3.5	5.2	0.25	0.16	191.1	74.1	3.47
400	500.0	19.0	48.7	33.3	0.72	0.56	755.0	226.8	8.52
750	763.1	23.2	92.4	43.7	1.04	0.62	1426.3	505.4	13.77
1000	942.1	45.6	123.6	48.2	1.28	0.60	2252.4	835.9	19.21

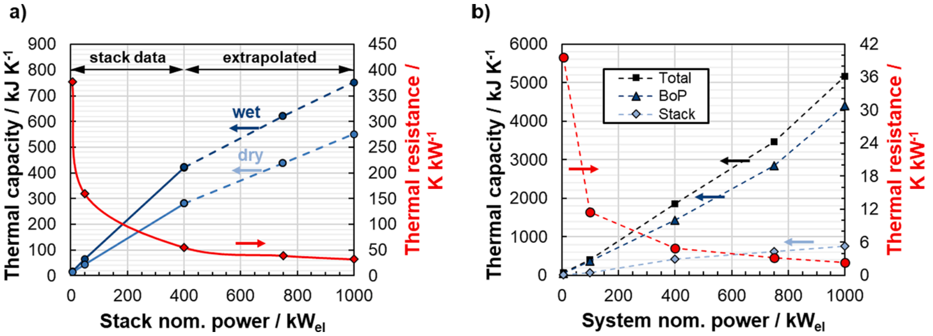

Fig. 2. Thermal capacities (blue) and thermal resistances (red) of electrolyzers with power ratings between 5 kW_{el} and 1 MW_{el} used in the simulations for: a) electrolysis stacks in dry state (light blue) and including the water content (dark blue); and b) the balance of plant (BoP), stacks, and total system. (For interpretation of the references to colour in this figure legend, the reader is referred to the web version of this article.)

analyzed firstly for heating powers with the benchmark ratings from Table 2, which represents a heating that is primed to maintain the operating temperature, and then heating powers that amount to 20 % of the electrical power rating of the electrolyzer. This considerable heating power represents the application of electrolysis systems as flexible heat sinks, such as in power-to-heat use cases. Additionally, in section 4.2.2, start-up with variable heat-input is considered for two strategies. Firstly, potentiostatic heat-up at 1.80 V cell voltage without additional heating is examined. Secondly, potentiostatic heat-up at 1.80 V, including additional heating with the benchmark heating powers from Table 2, is simulated to consider applications in which fast heat-up is paramount. For the sake of comparison, all simulations assume electrolyzers with 50 µm membranes, including the 100 kW_{el} system, which contrasts with the 200 µm membranes used in the reference experiments in section 4.1.

To generate general conclusions regarding electrolyzer heat-up efficiency, potentiostatic part-load start-up with cell voltages between 1.70 V and 2.00 V and heat-up using solely resistive electrical heating were simulated for all systems. These general results are discussed in section 4.2.3.

4. Results and discussion

4.1. *Experiments on the test station*

4.1.1. *Comparison of heat-up strategies*

The different strategies for accelerated heat-up of electrolyzers to 75 °C stated in Table 1 have been tested and compared energetically. The temperatures during heat-up are presented in Fig. 3 a). Heat-up using solely the additional heating is slowest with a total duration of 160 min. A gradual deceleration of the heat-up progression can be observed when the electrolyzer approaches its equilibrium temperature at the given heat input. Part-load operation substantially shortens the heat-up phase in the galvanostatic cases, resulting in 77 and 59 min for the 2- and 3-step strategies, respectively. Accordingly, increasing the number of steps accelerates electrolyzer heat-up, which can be explained by the greater input of heat from electrochemical dissipation. The deceleration effect, observed for the heating only case, can be compensated by the increased heat input and the temperature development is near linear. Operating the electrolyzers in potentiostatic mode with variable, increasing current density represents the limiting case with an infinite number of steps within the temperature range from 25 to 75 °C. The potentiostatic case at 1.80 V mean cell voltage without additional heating leads to a heat-up duration of 86 min and is thus only marginally faster than the 3-step case. Adding the additional heating to the potentiostatic operation results in the fastest heat-up of 53 min. Compared to the heating only case, this equals a 67 % faster start-up to nominal operating conditions.

The fastest heat-up duration may be interesting for some use cases, where the activation time is of the highest importance, but the individual efficiencies of the strategies should also be considered. Comparing the efficiencies based on the amount of energy to produce a fixed quantity of hydrogen after activation, as introduced through equations (18) to (21), can be performed. The results of the efficiency calculations can be seen in Fig. 3 b). In addition to the efficiencies, the production time until 1 kg of hydrogen is produced for each case is also depicted. Heating for only heat-up is the slowest case, taking a total of 239 min at the lowest efficiency of 56.1 %. Continued heat losses to ambient during heat-up also contribute to this. The galvanostatic 3-step

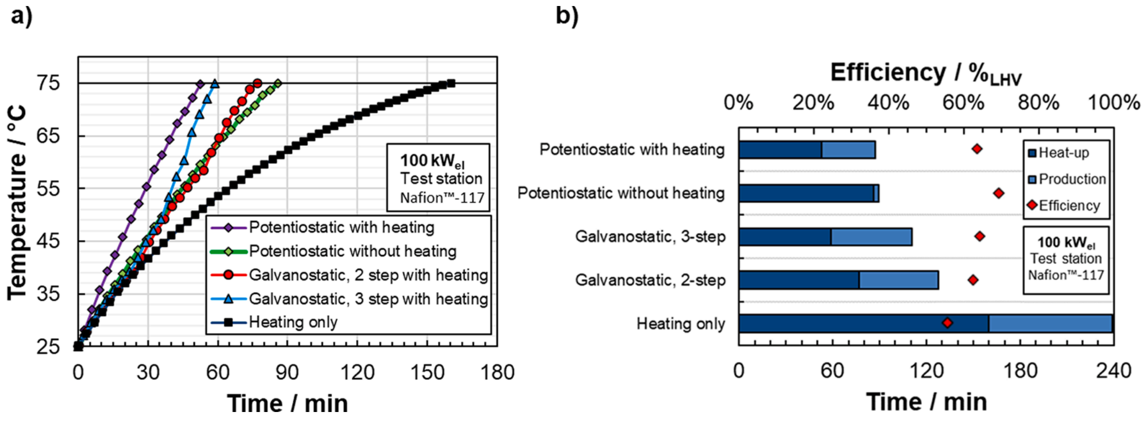

Fig. 3. Experimental comparison of different heat-up strategies from 25 °C to 75 °C temperatures at the 100 kW_{el} test station: a) temperature development over time; b) heat-up durations (dark blue), H_2 residuum production times (light blue), and heat-up effficiencies (red points). (For interpretation of the references to colour in this figure legend, the reader is referred to the web version of this article.)

case is not only faster than the 2-step one but also more efficient, at 64.3 %. Although potentiostatic heat-up with additional heating is much faster with respect to temperature, it takes almost as long to produce the first kilogram of hydrogen as potentiostatic heating without additional heating. Overall, the case of potentiostatic heat-up without additional heating has the highest efficiency of all investigated strategies, with 69.1 %. This efficiency is even higher than that of the nominal operating point because the efficiency of PEM electrolysis cells is higher at intermediate cell voltages.

Overall, the experiments show that amongst the tested heat-up procedures, potentiostatic heat-up is the most beneficial with respect to efficiency and ease of application. If the priority is on bringing the system to temperature as rapidly as possible, additional heat input from heating elements can be used. Otherwise, potentiostatic heat-up and the exploitation of electrochemical heat dissipation is more efficient and offers comparable hydrogen production rates.

4.1.2. Validation of the simulation model

Validation experiments were performed to test the agreement between the start-up behavior of the reference electrolyzer and the simulation model. Fig. 4 a) shows the results for heat-up experiments solely using the heating elements of 4 kW_{th} and potentiostatic heat-up with a cell voltage of 1.85 V and additional heating of 4 kW_{th}. For both cases, the simulation results match the experimental data sufficiently well. Based on the area below the temperature curves, an accuracy of 99.3 % was achieved. In plots of temperature over time, the integral below the plot is proportional to the thermal energy within the system.

In Fig. 4 a), the temperature curves exhibit slightly different curvatures, with the model overestimating the temperature by less than 1 K. Overall, the heat-up duration until 75 °C is predicted accurately is 162 min. In Fig. 4 b), the simulated temperature curve crosses the experimental curve after 36 min due to different curvatures. The predicted heat-up duration is 50 min, which is 5 min less than the measured time. Those differences occur due to deviations in the last 15 min of the experiments. These can be explained due to the influences of the temperature and power supply control that become apparent in periodic ripples of the temperature curve. Overall, the simulation model accurately predicts the heat-up process of the reference electrolyzer and can be used to examine other systems at various power scales.

4.2. Simulation of electrolyzer heat-up

Simulations of electrolyzer start-up at different scales were conducted to investigate this process with respect to different strategies. Firstly, a constant heat input by electrical heating was analyzed in a 400 kW_{el} system. Secondly, part-load operation and heating-based start-up strategies were compared regarding the heat-up times from 25 °C to 75 °C and the electrical energy required. Lastly, the dimensionless description of electrolyzer heat-up from (28) was applied to the gathered data.

4.2.1. Heat-up with constant heat input

Electrolyzers with an additional electrical heating may be brought to operating temperature without producing hydrogen. Appropriately dimensioning the heating is essential for obtaining efficient and economical electrolysis systems. Fig. 5 a) shows the results of simulations for a 400 kW_{el} electrolyzer and electrical heating powers from 12 kW_{th} to 80 kW_{th}. At a heating power of 12 kW_{th}, the temperature plot exhibits a pronounced curvature with a decreasing heat-up rate near 75 °C. This occurs because the thermal equilibrium at this heat input lies at 80 °C and the heat-up rate decreases near this temperature. Accordingly, the temperature plots straighten with increasing heating power and their curvature lessens, as can be observed in Fig. 5 a).

From these simulations, the heat-up times from 25 °C to 75 °C and the energy demand for heat-up can be determined. In Fig. 5 b), both quantities are plotted over the heating power for the 400 kW_{el} system. The heat-up time decreases from 157 min with a heating of 12 kW_{th}, to 59 min with 24 kW_{th}, and 16 min with 80 kW_{th}. At the same time, the energy demand for heat-up decreases with increasing heating power. Although heating with 12 kW_{th} requires 31.40 kWh of electricity for heat-up, the 20 kW_{th} heating requires 24.67 kWh and a heating with 80 kW_{th} uses 21.33 kWh. Shorter heat-up durations entail less aggregated heat losses, thus reducing the energy demand for heat-up. Although the linear heat-up ramps at high heat inputs further reduce the heat-up duration, the required energy demand diminishes less severely. This is due to the fixed quantity of thermal energy stored in the system, which depends on the heat capacity and remains unchanged by the heat-up procedure.

4.2.2. Start-up with variable heat input

The start-up procedures of water electrolyzers with power ratings of up to 1 MW_{el} are now compared using the simulation model and parameters presented in this article. In Fig. 6 a), the depicted data points represent the heat-up durations for four different start-up strategies.

As Fig. 6 a) shows, the heat-up of the electrolyzers was slowest when using the benchmark heating powers. With 162 and 157 min, respectively, the systems with 100 kW_{el} and 400 kW_{el} have similar heat-up durations. In comparison, electrolyzers with 750 kW_{el} and 1 MW_{el} require 273 and 294 min, respectively, to reach 75 °C. When equipped with electrical resistance heating elements amounting to 20 $\%_{nom}$, the electrolyzers take between 16 and 22 min to reach the set temperature. Thus, the installation of significant heating elements can qualify the use of electrolyzers as highly flexible heat sinks. In conjunction with subsequent hydrogen production, this power-to-heat application may

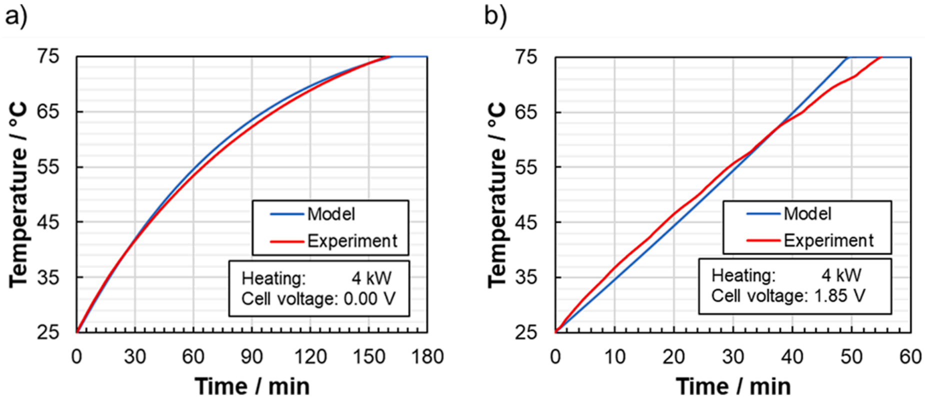

Fig. 4. Validation of the heat-up simulation model (blue) using experimental data from the 100 kW_{el} test station (red) for: a) heat-up using only the 4 kW_{th} heating; b) heat-up in part-load operation at 1.85 V cell voltage and additional 4 kW_{th} heating. (For interpretation of the references to colour in this figure legend, the reader is referred to the web version of this article.)

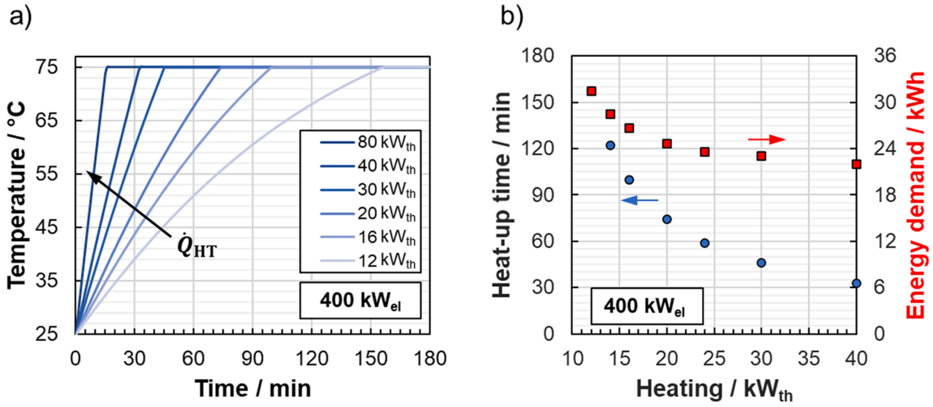

Fig. 5. Simulated heat-up of a 400 kW_{el} electrolyzer by electrical resistive heating with heat inputs between 12 kW_{th} and 80 kW_{th}: a) temperature development over time; b) heat-up times (blue) and total electrical energy demand during heat-up (red). (For interpretation of the references to colour in this figure legend, the reader is referred to the web version of this article.)

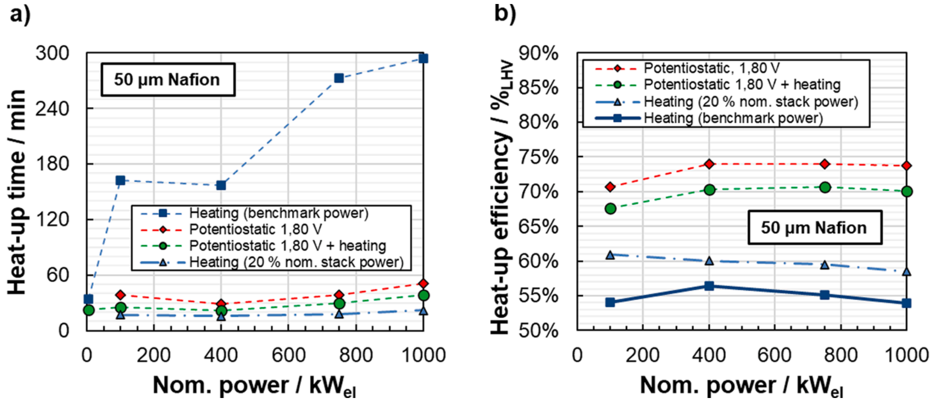

Fig. 6. Simulated heat-up for electrolyzers with power ratings between 5 kW_{el} and 1 MW_{el} using various start-up strategies and the benchmark heating powers from Table 2: a) heat-up times; b) heat-up efficiencies.

synergize well in existing installations. Similar heat-up durations result from potentiostatic part-load start-up, where they range from 16 to 22 min without additional heating. With benchmark heating powers, heat-up takes between 29 and 39 min for electrolyzers of up to 750 kW_{el} and 52 min for a 1 MW_{el} system. These part-load cases suggest that the effective start-up of electrolyzers can be achieved if intermediate cell voltages of 1.80 V are immediately required. Limiting the cell voltage during start-up also reduces degradation stresses on the stack components and electrolysis cells.

Table 5 lists the reference hydrogen quanta used for calculating the heat-up efficiency during start-up. These maximum hydrogen production masses were all obtained for the potentiostatic heat-up at 1.80 V cell voltage. At this cell voltage, the compromise between heat dissipation and hydrogen production efficiency is favorable.

Regarding the heat-up efficiencies at different scales as defined by (27), Fig. 6 b) conveys several conclusions. Firstly, potentiostatic heat-up at 1.80 V yields the highest heat-up efficiencies between 70.7 $\%_{LHV}$ and 74.0 $\%_{LHV}$, followed by potentiostatic heat-up, plus additional heating with efficiencies ranging from 67.6 $\%_{LHV}$ to 70.7 $\%_{LHV}$. Secondly, if using solely resistive electrical heating power for heat-up, the higher power ratings of the heating increase the heat-up efficiency. Hence, the strategy where the heating rating equals 20 % of the power rating of the electrolyzer results in significantly higher heat-up efficiencies of between 58.5 $\%_{LHV}$ and 60.9 $\%_{LHV}$. In comparison, the strategy with the benchmark heating only reaches heat-up efficiencies from 54.4 $\%_{LHV}$ to 56.4 $\%_{LHV}$. Thirdly, electrolyzers with power ratings of 400 kW_{el} and more exhibit approximately linear or similar behavior regarding their heat-up efficiencies and the 100 kW_{el} system deviates from that apart from the case with larger electrical heating. This effect is caused by the relative dissipative heat losses that are not compensated for by electrochemical heat production in smaller systems. Lastly, the tendency for decreasing heat-up efficiency with scale from 400 kW_{el} upwards is mainly due to the decreasing nominal electrolytical efficiency based on the nominal operating points of the electrolyzers and increasing heat losses.

Table 5
Reference hydrogen quanta obtained as the maximum hydrogen production during heat-up from 25 °C to 75 °C at 1.80 V constant cell voltage.

P_{nom} / kW_{el}	5	100	400	750	1000
$m_{H_2,max}$/ kg	0.15	0.73	2.81	5.57	9.61

Fig. 7 a) depicts the simulated energy demands for the various heat-up strategies. Potentiostatic heat-up at 1.80 V requires the most energy, of up to 434 kWh, for the 1 MW_{el} electrolyzer. Slightly less electrical energy is required with potentiostatic heat-up and additional heating as the shorter heat-up phase in these cases means lower aggregated heat losses and faster reaching of the nominal operating point. With the increasing power rating of the electrolyzer, the difference between potentiostatic heat-up with and without additional heating increases. This relates to similar behaviors of the heat-up durations, as is apparent in Fig. 7 a), that are caused by the increasing thermal capacity of the entire electrolysis system with scale in Fig. 2 b). Heat-up based on electrical heating elements requires significantly less energy, as the energy for hydrogen production is not included. Furthermore, the necessary energy demand reduces with increasing heat input, as

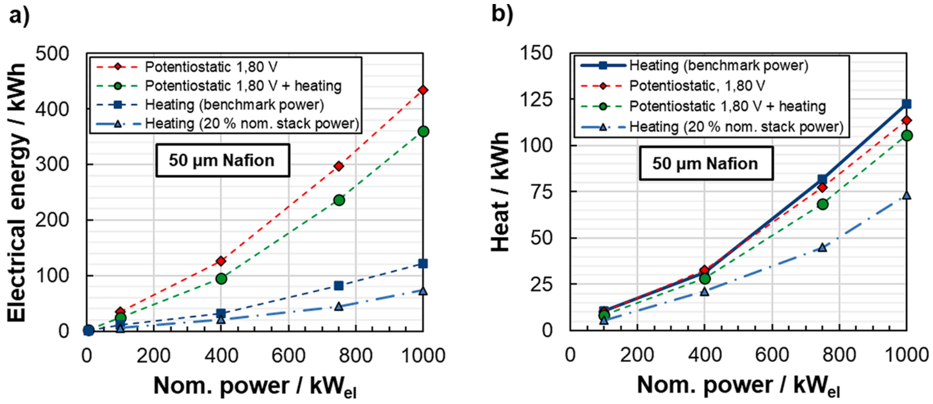

Fig. 7. Simulated heat-up for electrolyzers with power ratings between 5 kW_{el} and 1 MW_{el} using various start-up strategies and the benchmark heating powers from Table 2: a) total electrical energy demand; b) heat input during heat-up.

demonstrated by the plots of the heating-based strategies in Fig. 7 a).

Regardless of the applied start-up strategy, the thermal energy stored within the system is determined by its thermal masses. Heat losses to ambient, however, accumulate during heat-up and lead to different total amounts of required heat. Hence, in Fig. 7 b), heat-up with heating ratings of 20 % of the electrical power rating of the electrolyzer, which represents the highest heat input of all the strategies considered in this study, requires by far the lowest amount of heat. Inversely, heating with the benchmark heating ratings requires more heat than all other heat-up scenarios. This is due to the low heat input and long heat-up process in that case. For electrolyzers with power ratings of up to750 kW_{el}, potentiostatic heat-up at 1.80 V without additional heating involves similar heat demands as the benchmark heating case, although the heat-up efficiency is much higher, as previously discussed. Using additional heating during potentiostatic heat-up at 1.80 V shortens the heat-up duration and reduces the heat demand. This effect becomes more pronounced for electrolyzers with power ratings greater than 400 kW_{el}.

4.2.3. Dimensionless comparison

All of the results presented can be compared on a dimensionless basis by using the concept of the heat-up number and dimensionless heat-up time, as introduced by (28) and (30). Every data point in Fig. 8 represents the results of a simulation run, with the benefit of allowing the comparison of different electrolyzers at all scales in one plot. Further analysis of the respective parameters pertaining to the data points shows clustering of the efficiencies of certain heat-up strategies. The dashed lines and annotations in Fig. 8 represent the different clusters and highlight the utilized start-up case.

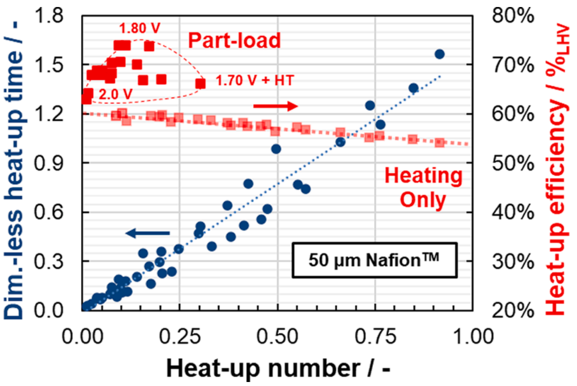

Fig. 8. Dimensionless comparison of the simulation results for heat-up times (blue) and heat-up efficiencies (red) of electrolyzers with up to 1 MWel using 50 µm Nafion™ membranes. (For interpretation of the references to colour in this figure legend, the reader is referred to the web version of this article.)

The dimensionless heat-up number and heat-up times approximately follow a linear relationship ($R^2 = 0.958$), especially for low heat-up numbers, which characterize cases of high heat inputs. This observation is consistent with the results for various heat inputs – for example in Fig. 5 – where high heat input yields constant heat-up rates, whereas low heat inputs cause curved temperature plots with decreasing heat-up rates. As the heat-up number essentially linearizes the heat-up phase of electrolyzers, the accuracy of prediction is therefore better for high heat inputs.

In Fig. 5, a linear relationship between the heating-based heat-up and heat-up number ($R^2 = 0.926$) is apparent. With an increasing heat-up number, the heat-up efficiency decreases, indicating favorable efficiency at low heat-up numbers, which results from high heat inputs. This is congruent with other results presented herein. Extrapolating the linear approximation for the heating-only case to a heat-up number of zero, a maximum heat-up efficiency of 61 $\%_{LHV}$ can be estimated. In all cases, part-load start-up yields higher efficiencies than heating-only. At a 1.80 V cell voltage, without further heating, the highest heat-up efficiency of 74.0 $\%_{LHV}$ is reached. Lower voltages result in decreased efficiency, with 1.90 V without heating, as in the case of 1.70 V with additional heating. At 2.0 V, the efficiency decreases further, approaching that of the heating-based strategies. This is due to the decreased cell efficiency during start-up.

5. Conclusions

From the findings of this study, several conclusions can be drawn for the start-up phase of PEM water electrolyzers. These should also be applicable to other low-temperature electrolysis technologies such as alkaline or anion exchange electrolyzers. A framework for the fair energetic comparison of heat-up processes was laid, including the definition of the heat-up efficiency, dimensionless heat-up number, and heat-up time. A simulation model for electrolyzer start-up was developed and experimentally-validated in a 100 kW_{el} PEM electrolyzer. From experiments and simulations, it was concluded that part-load heat-up is the most efficient, reaching maximum efficiencies of up to 74.0 $\%_{LHV}$ at 1.80 V. For operators of electrolyzers, this means that they should limit the cell voltage during heat-up – if possible – to maximize hydrogen production during this phase and further mitigate accelerated cell degradation at higher cell potentials. In comparison, heat-up using only electrical resistive heating is less efficient, at only up to 61 $\%_{LHV}$. However, heat-up efficiency increases with heating power by reducing aggregating heat losses to ambient. Moreover, promising use cases of electrolyzers might arise if they are equipped with heating elements to qualify them as heat sinks in electricity grids with temporary overproduction of up to 15 min.

CRediT authorship contribution statement

Edward Rauls: Conceptualization, Methodology, Software, Writing – original draft, Visualization. **Michael Hehemann:** Methodology, Resources, Writing – review & editing. **Roger Keller:** Resources, Writing – review & editing. **Fabian Scheepers:** Writing – review & editing. **Martin Müller:** Conceptualization, Writing – review & editing, Supervision. **Detlef Stolten:** Supervision.

Declaration of Competing Interest

The authors declare that they have no known competing financial interests or personal relationships that could have appeared to influence the work reported in this paper.

Data availability

The authors are unable or have chosen not to specify which data has been used.

Acknowledgements

This work was supported by the state of North Rhine–Westphalia with funds from the European Regional Development Fund (ERDF) as part of the project, "Kompetenz-Zentrum Virtuelles Institut Strom zu Gas und Waerme" (Grant No. EFRE-0400151) and by the Deutsche Forschungsgemeinschaft (DFG, German Research Foundation) - 491111487. The authors would also like to thank Saanika Deokule, Lukas Ritz and Richard Wegner for their support of the experiments.

All authors have read and agreed to the published version of the manuscript.

Appendix

Nomenclature.

Latin symbols	Meaning Unit
a	activity -
C	thermal capacitance kJ/K^{-1}
c	thermal capacity kJ/mol^{-1} K^{-1}
d	thickness mm
E	energy J
F	Faraday number As/mol^{-1}
G	Gibbs energy kJ/mol^{-1}
H	enthalpy kJ/mol^{-1}
I	current A
j	current density A cm^{-2}
LHV	lower heating value kJ kg^{-1}
m	mass kg
n	amount of substance mol
	number of cells -
p	pressure Pa
P	permeability mol cm^{-1} Pa^{-1} s^{-1}
Q	heat kJ
R	universal gas constant kJ/mol^{-1} K^{-1}
	Ohmic resistance Ω
S	entropy kJ/K
	surface m^2
T	temperature K
t	time s
U	voltage V
z	number of electrons -
Greek symbols	**Meaning Unit**
α	charge transfer coefficient -
	heat transfer coefficient kJ m-2 K-1
η	efficiency %
	overpotential V
φ	relative humidity %
σ	protonic conductivity S cm-1
τ	time constant s
Subscripts	**Meaning**
0	at standard conditions
act	activation
amb	ambient
an	anode
cat	cathode
el	electric
H_2	hydrogen
HT	heating
mem	membrane
nom	nominal
O_2	oxygen
ohm	Ohmic
Ω	Ideal ohmic
OV	overvoltage

(*continued on next page*)

(*continued*)

Latin symbols	Meaning Unit
ref	reference
res	residual
rev	reversible
th	thermal
vap	vapor
w	water
wt	gravimetric

References

[1] Zappa W, Junginger M, van den Broek M. Is a 100% renewable European power system feasible by 2050? Appl Energy 2019;233–234:1027–50.

[2] Beevers D, Branchini L, Orlandini V, de Pascale A, Perez-Blanco H. Pumped hydro storage plants with improved operational flexibility using constant speed Francis runners. Appl Energy 2015;137:629–37.

[3] Díaz-González F, Hau M, Sumper A, Gomis-Bellmunt O. Coordinated operation of wind turbines and flywheel storage for primary frequency control support. Int J Electr Power Energy Syst 2015;68:313–26.

[4] Bullich-Massagué E, Cifuentes-García F-J, Glenny-Crende I, Cheah-Mañé M, Aragüés-Peñalba M, Díaz-González F, et al. A review of energy storage technologies for large scale photovoltaic power plants. Appl Energy 2020;274.

[5] He W, Luo X, Evans D, Busby J, Garvey S, Parkes D, et al. Exergy storage of compressed air in cavern and cavern volume estimation of the large-scale compressed air energy storage system. Appl Energy 2017;208:745–57.

[6] Chowdhury JI, Balta-Ozkan N, Goglio P, Hu Y, Varga L, McCabe L. Techno-environmental analysis of battery storage for grid level energy services. Renew Sustain Energy Rev 2020;131:110018.

[7] Blanco H, Nijs W, Ruf J, Faaij A. Potential for hydrogen and Power-to-Liquid in a low-carbon EU energy system using cost optimization. Appl Energy 2018;232:617–39.

[8] van Leeuwen C, Mulder M. Power-to-gas in electricity markets dominated by renewables. Appl Energy 2018;232:258–72.

[9] Petkov I, Gabrielli P. Power-to-hydrogen as seasonal energy storage: an uncertainty analysis for optimal design of low-carbon multi-energy systems. Appl Energy 2020;274:115197.

[10] Carmo M, Fritz DL, Mergel J, Stolten D. A comprehensive review on PEM water electrolysis. Int J Hydrogen Energy 2013;38(12):4901–34.

[11] Bareiß K, La Rua C de, Möckl M, Hamacher T. Life cycle assessment of hydrogen from proton exchange membrane water electrolysis in future energy systems. Applied Energy 2019;237:862–72.

[12] Welder L, Stenzel P, Ebersbach N, Markewitz P, Robinius M, Emonts B, et al. Design and evaluation of hydrogen electricity reconversion pathways in national energy systems using spatially and temporally resolved energy system optimization. Int J Hydrogen Energy 2019;44(19):9594–607.

[13] Papadopoulos V, Desmet J, Knockaert J, Develder C. Improving the utilization factor of a PEM electrolyzer powered by a 15 MW PV park by combining wind power and battery storage – Feasibility study. Int J Hydrogen Energy 2018;43(34):16468–78.

[14] Da Nascimento SG, Rochedo PR, Szklo A. Renewable hydrogen production to deal with wind power surpluses and mitigate carbon dioxide emissions from oil refineries. Appl Energy 2022;311:118631.

[15] Bhaskar A, Assadi M, Nikpey SH. Decarbonization of the Iron and Steel Industry with Direct Reduction of Iron Ore with Green Hydrogen. Energies 2020;13(3):758.

[16] Faria JA. Renaissance of ammonia synthesis for sustainable production of energy and fertilizers. Curr Opin Green Sustainable Chem 2021;29:100466.

[17] Saba SM, Müller M, Robinius M, Stolten D. The investment costs of electrolysis – A comparison of cost studies from the past 30 years. Int J Hydrogen Energy 2018;43(3):1209–23.

[18] Taner T, Naqvi SAH, Ozkaymak M. Techno-economic Analysis of a More Efficient Hydrogen Generation System Prototype: A Case Study of PEM Electrolyzer with Cr-C Coated SS304 Bipolar Plates. Fuel Cells 2019;19(1):19–26.

[19] Schmidt O, Gambhir A, Staffell I, Hawkes A, Nelson J, Few S. Future cost and performance of water electrolysis: An expert elicitation study. Int J Hydrogen Energy 2017;42(52):30470–92.

[20] Chase MW. NIST-JANAF Thermochemical Tables. J. Phys. Chem. Ref. Data: Monograph; 1998. p. 9.

[21] Harrison KW, Hernández-Pacheco E, Mann M, Salehfar H. Semiempirical Model for Determining PEM Electrolyzer Stack Characteristics. J Fuel Cell Sci Technol 2006;3(2):220–3.

[22] Jerkiewicz G. Standard and Reversible Hydrogen Electrodes: Theory, Design, Operation, and Applications. ACS Catal 2020;10(15):8409–17.

[23] Bernt M, Gasteiger HA. Influence of Ionomer Content in IrO 2 /TiO 2 Electrodes on PEM Water Electrolyzer Performance. J Electrochem Soc 2016;163(11):F3179–89.

[24] Biaku C, Dale N, Mann M, Salehfar H, Peters A, Han T. A semiempirical study of the temperature dependence of the anode charge transfer coefficient of a 6kW PEM electrolyzer. Int J Hydrogen Energy 2008;33(16):4247–54.

[25] Springer TE. Polymer Electrolyte Fuel Cell Model. J Electrochem Soc 1991;138(8).

[26] Hwang GS, Parkinson DY, Kusoglu A, MacDowell AA, Weber AZ. Understanding Water Uptake and Transport in Nafion Using X-ray Microtomography. ACS Macro Lett 2013;2(4):288–91.

[27] Ito H, Maeda T, Nakano A, Takenaka H. Properties of Nafion membranes under PEM water electrolysis conditions. Int J Hydrogen Energy 2011;36(17):10527–40.

[28] Yadav R, Fedkiw PS. Analysis of EIS Technique and Nafion 117 Conductivity as a Function of Temperature and Relative Humidity. J Electrochem Soc 2012;159(3):B340–6.

[29] Stähler M, Stähler A, Scheepers F, Carmo M, Stolten D. A completely slot die coated membrane electrode assembly. Int J Hydrogen Energy 2019;44(14):7053–8.

[30] Ulleberg O. Modeling of advanced alkaline electrolyzers: a system simulation approach. Int J Hydrogen Energy 2003;28:21–33.

[31] Incropera F, Dewitt D, Bergman T, Lavine A. Fundamentals of Heat and Mass Transfer. 6th ed.: John Wiley & Sons; 2007.

[32] Scheepers F, Stähler M, Stähler A, Rauls E, Müller M, Carmo M, et al. Improving the Efficiency of PEM Electrolyzers through Membrane-Specific Pressure Optimization. Energies 2020;13(3).

[33] Rakousky C, Reimer U, Wippermann K, Kuhri S, Carmo M, Lueke W, et al. Polymer electrolyte membrane water electrolysis: Restraining degradation in the presence of fluctuating power. J Power Sources 2017;342:38–47.

[34] Scheepers F, Stähler M, Stähler A, Rauls E, Müller M, Carmo M, et al. Temperature optimization for improving polymer electrolyte membrane-water electrolysis system efficiency. Appl Energy 2020.

[35] Lettenmeier P, Wang L, Golla-Schindler U, Gazdzicki P, Cañas NA, Handl M et al. Nanosized IrO(x)-Ir Catalyst with Relevant Activity for Anodes of Proton Exchange Membrane Electrolysis Produced by a Cost-Effective Procedure. Angewandte Chemie (International ed. in English) 2016;55(2):742–6.

[36] Onda K, Kyakuno T, Hattori K, Ito K. Prediction of production power for high-pressure hydrogen by high-pressure water electrolysis. J Power Sources 2004;132(1–2):64–70.

[37] Schalenbach M, Hoefner T, Paciok P, Carmo M, Lueke W, Stolten D. Gas Permeation through Nafion. Part 1: Measurements. J Phys Chem C 2015;119(45):25145–55.

[38] Schröder V, Emonts B, Janßen H, Schulze H-P. Explosion Limits of Hydrogen/Oxygen Mixtures at Initial Pressures up to 200 bar. Chem Eng Technol 2004;27(8):847–51.

[39] García-Valverde R, Espinosa N, Urbina A. Simple PEM water electrolyser model and experimental validation. Int J Hydrogen Energy 2012;37(2):1927–38.

[40] Mills KC, Su Y, Li Z, Brooks RF. Equations for the Calculation of the Thermo-physical Properties of Stainless Steel. ISIJ Int 2004;44(10):1661–8.

[41] Stevens R, Boerio-Goates J. Heat capacity of copper on the ITS-90 temperature scale using adiabatic calorimetry. J Chem Thermodyn 2004;36(10):857–63.

[42] Velisaris CN, Seferis JC. Heat Transfer Effects on the Processing – Structure Relationships of Polyetheretherketone (Peek) Based Composites. Sci Eng Compos Mater 1988;1:13–22.

[43] Angell CA, Sichina WJ, Oguni M. Heat capacity of water at extremes of supercooling and superheating. J Phys Chem 1982;86(6):998–1002.